

Section 2

PROGRESS IN LASER FUSION

2.A Temporal Dependence of the Mass-Ablation Rate in UV-Laser-Irradiated Spherical Targets

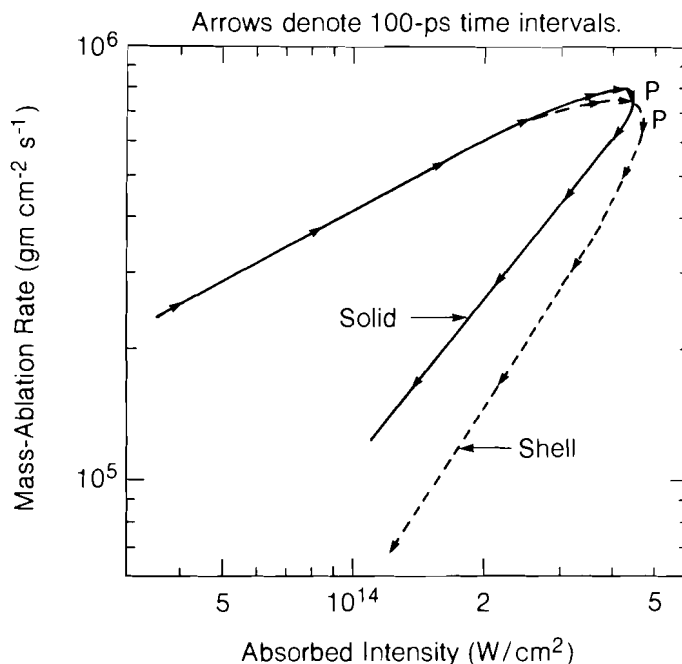
Thermal transport in spherical targets, uniformly irradiated with multiple, nanosecond-duration laser beams, has been a topic of much theoretical¹ and experimental interest.²⁻⁶ Understanding thermal transport is important in that it directly affects laser-induced ablation processes, which drive the implosion of direct-drive laser-fusion targets. The direct measurement of the transport of thermal energy from the absorption region to the ablation surface is not possible. However, the mass-ablation rate, \dot{m} (gm/cm²-s), which is very closely related to thermal transport and is a measure of the depth of material penetrated by the heat front during the laser pulse, can be measured through a variety of diagnostics, such as plasma velocity and x-ray spectroscopic techniques.

There is a growing body of experimental measurements of \dot{m} , some of which appear to suggest that the transport of thermal energy is inhibited. Computer simulations of these experiments place an upper limit on the heat flux q ,⁷ such that $q = \min(q_{c1}, f q_{fs})$, where q_{c1} is the classical value, q_{fs} is the free-streaming limit, and f is referred to as the flux limiter. Experiments in spherical geometry have inferred various levels of flux inhibition. With $\lambda = 1.05\text{-}\mu\text{m}$ laser irradiation,^{2,5} values range from as low as $f = 0.06$ to values in excess of the free-streaming limit. In Ref. 4, a low-temperature foot on the heat front was observed that cannot be explained with a simple flux-limited inhibition model. At $\lambda = 0.53\ \mu\text{m}$,² a flux limiter of $f > 0.1$ has been inferred. In experiments at $\lambda = 0.35\ \mu\text{m}$,⁶ the charge collector versus time-integrated x-ray spectroscopy measurements show markedly different values of \dot{m} and of its scaling with absorbed intensity I_A .

This broad range of inferred flux limiters from apparently similar experiments is difficult to reconcile. The inconsistency could be due to differences in experimental parameters, such as laser pulse shape and irradiation geometry and uniformity. Other factors, such as the shorter scale lengths on smaller targets and the onset of resonant absorption at higher intensities, will also affect thermal transport. Further, important consideration must be given to the influence of time-dependent effects. The time dependence of the mass-ablation rate and its scaling with absorbed intensity have been examined here using the first 6 and 12 UV-converted beams of OMEGA, and the results have been compared with computer simulations.

Computer Simulations of \dot{m}

In Fig. 23.12, we present the instantaneous mass-ablation rate during a pulse as a function of the instantaneous absorbed intensity (referenced to the original target diameter) as calculated by the one-dimensional (1-D) Lagrangian code *L/LAC*.⁸ Laser parameters were $\lambda = 0.351 \mu\text{m}$, power = 2.5 TW, Gaussian pulse shape with a 600-ps FWHM, and tangential focusing conditions, producing an incident intensity $I_0 = 5 \times 10^{14} \text{ W/cm}^2$ on a 404- μm -diameter target. Code simulations include ray tracing using the azimuthally averaged laser spatial profile, radiation transport with LTE opacities, and heat flux as the harmonic mean of q_{cl} and $f q_{\text{fs}}$. Simulations were run for a variety of flux limiters ranging from $f = 0.02$ to $f = 0.4$. The case for $f = 0.1$ is



E3440

Fig. 23.12
 LILAC simulation for the instantaneous mass-ablation rate [from Eq. (1)] versus the instantaneous absorbed intensity during a single laser pulse, $I_0 = 5 \times 10^{14} \text{ W/cm}^2$, $f = 0.1$ on 404- μm -diameter glass targets; solid target (—), 6- μm -wall shell target (- - -). Arrows mark 100-ps time intervals starting at 200-ps code time, and P denotes the peak of the laser pulse at 773 ps.

illustrated in Fig. 23.12 for a solid glass sphere and a 6- μm -thick glass shell target. The mass-ablation rate was calculated by following the progress of the 500-eV isotherm, as referenced to the original Lagrangian frame.

$$\dot{m} = \rho \Delta r / \Delta \tau \quad (1)$$

where ρ is the material density, and Δr is the thickness of material progressively heated to 500 eV in a time $\Delta \tau$. The 500-eV isotherm was chosen as a characteristic temperature for Si line emission in the 2.0- to 2.5-keV range, which was used as a diagnostic in the experiments described later. The value of $\dot{m}(t)$ derived from the 300-eV or 1-keV isotherm is essentially the same as for the 500-eV isotherm, with peak values occurring marginally earlier and later in time, respectively. This is characteristic of the steep classical heat front in the overdense material.

The noteworthy features of the curves in Fig. 23.12 are that \dot{m} does not have the same scaling with absorbed intensity (I_A) on the rising and falling edges of the laser pulse and that the peak value of \dot{m} is achieved prior to the peak values of both the incident and absorbed intensities. These features are even more pronounced for the glass shell compared to the solid target. A similar dependence of \dot{m} on I_A has been observed in simulations with other flux limiters, as well as for targets of different diameters and different Z .

Our efforts to use the simulations to generate scaling laws of the form $\dot{m} \propto I_A^X R_A^Y$ (as in Ref. 1), where R_A is the 500-eV isotherm radius, have been successful only for individual cases and then only for moving-shell targets. On solid glass spheres the excursion of R_A during the laser pulse may range up to 30% of the initial target radius, but it cannot account for the observed decrease in \dot{m} . Larger excursions are observed for higher-intensity laser pulses ($5 \times 10^{15} \text{ W/cm}^2$) and for smaller (200- μm)-diameter targets.

At $\lambda = 0.351 \mu\text{m}$, the predominant absorption mechanism is inverse bremsstrahlung in the subcritical region, and we can define an energy deposition radius R_D as the weighted average absorption radius. Typically, R_D lies between the critical and quarter-critical density radii, but inside the peak temperature ($\nabla T = 0$) surface. Defining $\Delta R = R_D - R_A$ as the separation between the energy deposition and ablation surfaces, we find the scaling laws for glass targets

$$\dot{m} \propto I_A^{0.5} \times R_A^{1.4} \times \Delta R^{-0.06} \quad \text{for } f = 0.02$$

$$\dot{m} \propto I_A^{0.65} \times R_A^{1.3} \times \Delta R^{-0.3} \quad \text{for } f = 0.04$$

$$\text{and } \dot{m} \propto I_A \times R_A \times \Delta R^{-0.73} \quad \text{for } f = 0.40$$

The scaling at $f = 0.1$ is similar to that at $f = 0.4$. The magnitude of ΔR is partially dependent on the target size and composition. For moving-shell targets ΔR increases monotonically throughout the laser pulse, but

for solid spheres ΔR is approximately constant after the peak of the laser pulse. We also note that ΔR is proportional to the density scale length L_D at R_D – and perhaps L_D is a more meaningful parameter for the scaling laws, as it affects energy deposition in the corona directly. Another factor that contributes to decreasing \dot{m} is that the fraction of the absorbed energy deposited outside the $\nabla T = 0$ surface increases during the laser pulse.

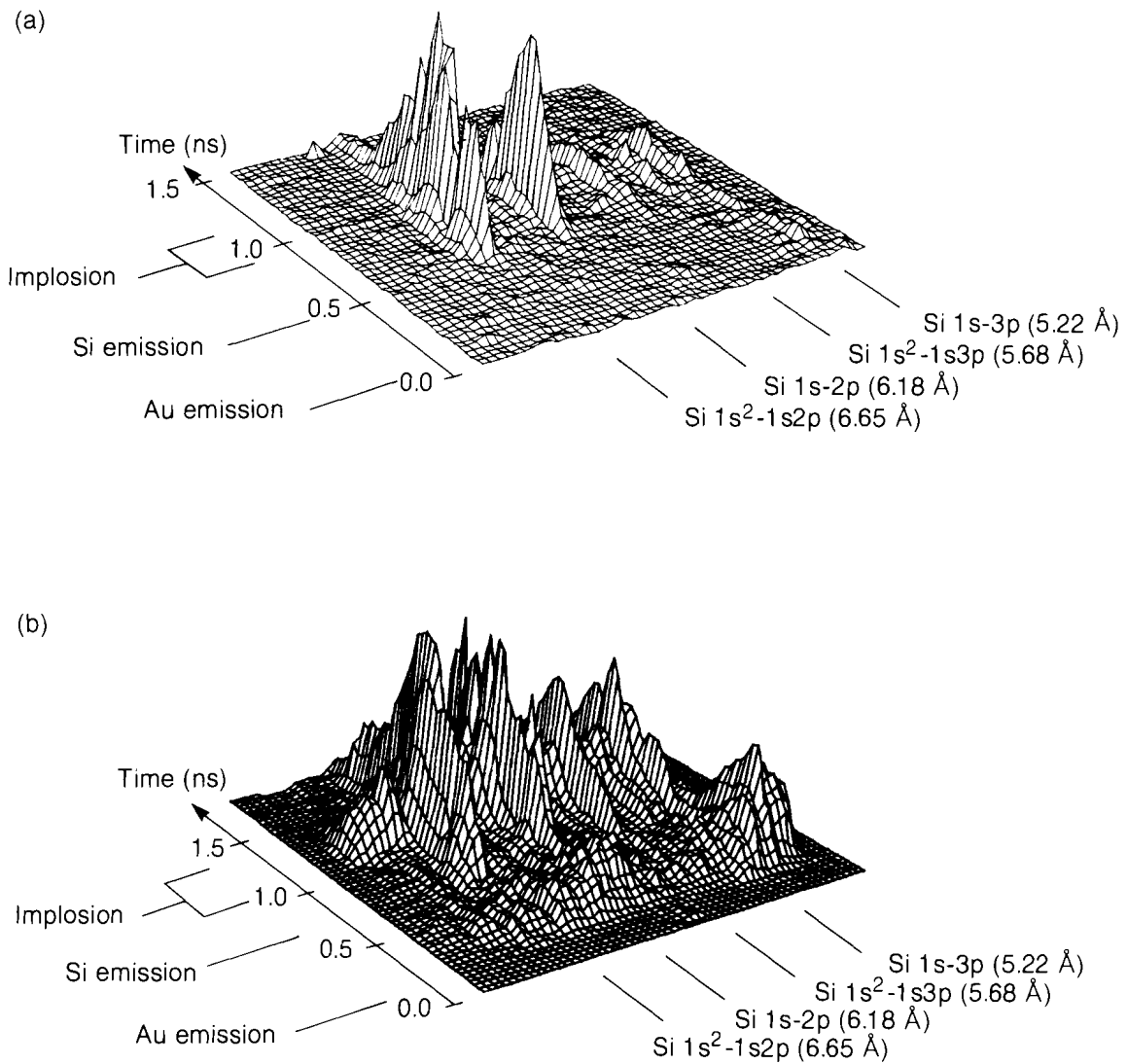
As suggested in Ref. 1, inverse bremsstrahlung leads to reduced \dot{m} and reduced ablation pressure compared to an energy dump at critical density. More of the laser energy is dissipated at subcritical densities, flowing more directly into blowoff kinetic energy. Also, ΔR is larger because R_D is larger. From Ref. 1 we note that the ablation pressure has a much weaker scaling with radius than \dot{m} does, and our simulations do show that the pressure at the 500-eV isotherm scales with I_A on both the leading and trailing edges of the pulse for the solid targets.

In light of the above simulations, care must be taken when plotting \dot{m} obtained from time-resolved x-ray spectroscopy versus absorbed intensity. Using a pulse-averaged I_A will result in an underestimate in the value of \dot{m} (I_A). To avoid such problems, the time-varying values of \dot{m} should be plotted using the instantaneous value of I_A .

Experiments

The primary diagnostic for our mass-ablation-rate measurements was time-resolved x-ray spectroscopy.^{9,10} The experiments were carried out using 6 and 12 UV ($\lambda = 0.351\text{-}\mu\text{m}$) beams of the OMEGA laser system at incident irradiances of $I_o = 1 \times 10^{14}$ to 4×10^{14} W/cm². The laser pulse had a Gaussian temporal profile with a 600- to 750-ps FWHM. Two types of targets were used in these studies. One set consisted of empty glass microballoons ($\sim 230\text{-}\mu\text{m}$ diameter) with a $1\text{-}\mu\text{m}$ -thick wall. These shells were coated with CH (1- to $8\text{-}\mu\text{m}$ thick) and then overcoated with a $150\text{-}\text{\AA}$ layer of Au to provide an initial x-ray time marker. The thickness of the Au layer was increased to 300 \AA for the 12-beam target shots. The second set of targets were solid glass spheres ($\sim 200\text{-}\mu\text{m}$ diameter) coated with three layers: $1.5\text{-}\mu\text{m}$ CH, $0.05\text{-}\mu\text{m}$ Al, and $1.5\text{-}\mu\text{m}$ CH.

An elliptically curved PET crystal analyzer was used to disperse the x-ray spectrum (1.7- to 2.7-keV range) onto the slit of the x-ray streak camera. Spectral and temporal resolutions were $E/\Delta E \sim 600$ and 15 ps, respectively. Perspective plots of the x-ray intensity from streak records for 6- and 12- beam target shots, showing the Au and Si line emission and the implosion time, are presented in Fig. 23.13. The mass-ablation rate through the CH layers of known thickness was measured from the time delay between the start of the Au or Al line emission to the onset of the Si emission from the glass substrate. In all of the target shots where we could measure \dot{m} , the CH layer ablated during the rising edge of laser pulse. Thicker CH layers ($6\text{-}8\text{ }\mu\text{m}$) did not appear to burn through.



E3441

Fig. 23.13

Perspective plots of the x-ray intensity, as recorded by the streak camera. Correction for the spectrometer response function would increase the intensity on the long-wavelength side by 40%.

(a) 150-Å Au on 4- μm CH on 1.0- μm glass shell target. Diameter is 229 μm at $I_0 = 2.8 \times 10^{14} \text{ W/cm}^2$ with 6-beam irradiation.

(b) 300-Å Au on 3- μm CH on 1.0- μm glass shell target. Diameter is 289 μm at $I_0 = 4.2 \times 10^{14} \text{ W/cm}^2$ with 12-beam irradiation.

In order to construct a meaningful plot of \dot{m} versus I_A , we require knowledge of the absorbed laser intensity during the CH burn-through time of interest. This was inferred from careful comparisons of the streak data with the LILAC code simulations, since we could not measure directly the absorption fraction as a function of time nor relate the x-ray emission to the incident laser pulse. We assumed that if the overall predicted absorption of the laser energy agreed with the experimental measurement, then the code could be relied upon to predict the instantaneous absorbed laser intensity during the pulse. Typically, a flux limiter of $f = 0.04$ was required to match the absorbed fractions. We also assumed that the hydrodynamic implosion time predicted by the code for the shell targets was correct. Knowledge of the implosion time allowed us to relate the x-ray emission on the streak record to the incident laser pulse, because the implosion of the glass shell produces a broad and intense spectral feature on the x-ray streak records. This x-ray burst is characteristic of the higher temperatures and densities achieved during the stagnation of the glass shell and lasts ~ 150 ps. The accuracy of the implosion time was checked by calculating the predicted absorbed laser energy up to a time corresponding to the onset of the Au emission, as measured on the streak record. The calculated absorbed laser energy was in the range 3.0 – 5.5 J (Fig. 23.14), which corresponds to a time window of ~ 80 ps. Conservatively, this implies a 100-ps accuracy on our timing fiducial technique. By including a ± 50 -ps jitter in the streak record timing, we obtain a timing fiducial with 150-ps accuracy for the solid-sphere targets.

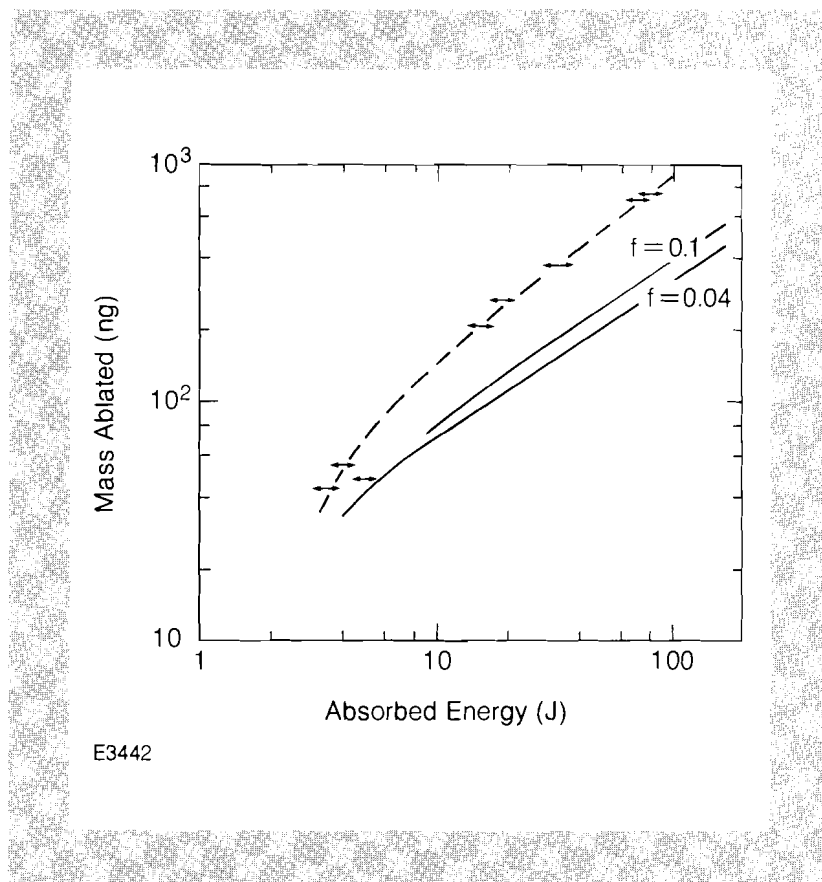


Fig. 23.14
 Ablated mass versus absorbed energy for 6-beam irradiation of multilayer targets. The total mass outside the glass substrate is assumed to have been ablated. Solid lines are LILAC simulations for the mass outside the 500-eV isotherm. Data points at ~ 4 J absorbed energy are for the ablation of the outer Au layer only.

In Fig. 23.15, we present the scaling of the measured mass-ablation rate versus the average absorbed laser intensity during the CH burn-through interval; I_A is derived from the simulations as outlined above. We also include data for \dot{m} for the outer CH layer on the solid targets where I_A is derived using 3 J of absorbed energy for time zero. The time-resolved 6-beam data is in excellent agreement with the time-integrated measurements at $I_A = 7.5 \times 10^{13}$ W/cm², which was measured for a similar target diameter.⁶ The scaling of \dot{m} with I_A for 6-beam irradiation and $I_A \leq 10^{14}$ W/cm² is in reasonable agreement with code predictions, although the magnitude of \dot{m} is a factor of 2 higher than that predicted for uninhibited transport ($f = 0.4$). The scaling of \dot{m} with I_A derived from the time-integrated x-ray spectroscopy of Ref. 6 is much weaker than reported here.

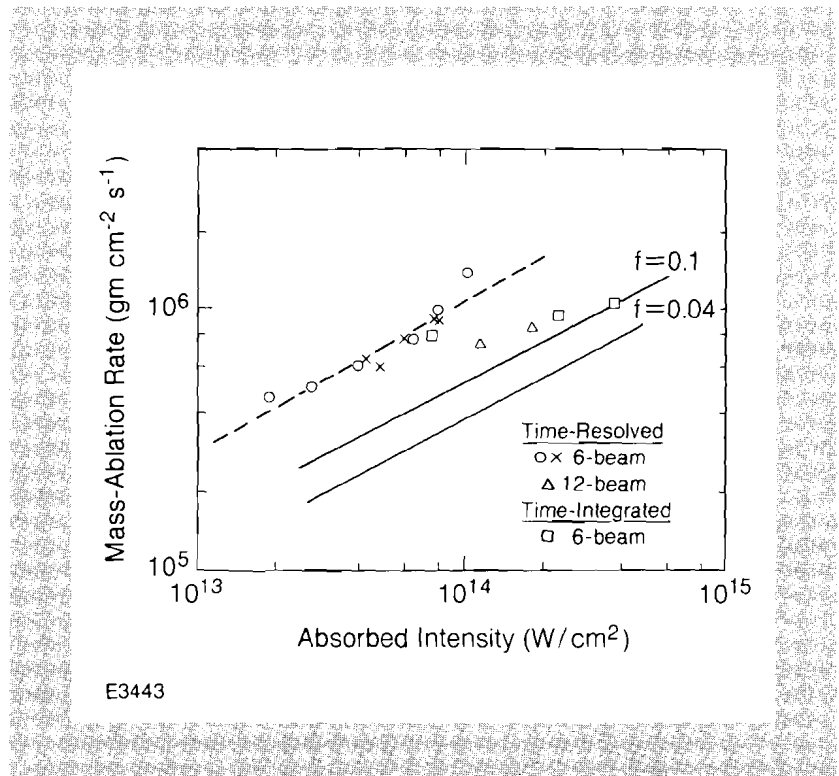


Fig. 23.15
Mass ablation rate versus absorbed intensity at $\lambda = 0.351 \mu\text{m}$. Compared are results from this study (---), time-integrated measurements from Ref. 6, and LILAC simulations at $f=0.1$ and $f=0.04$ for the rising edge of the pulse.

Part of the discrepancy in the measured and calculated values of \dot{m} can be attributed to irradiation nonuniformities. X-ray pinhole pictures of the targets irradiated with 6 beams have shown large-scale x-ray intensity variations across the target surface.¹¹ Time-resolved imaging of the x-ray emission from the target has also confirmed the existence of discrete hot spots. A detailed computation of the irradiation uniformity on target using measured beam profiles shows that a few percent of the laser energy is absorbed at an intensity greater than three times the average intensity.¹² Given the amount of energy in the hot spots and the sensitivity of our diagnostic—Au emission can be detected with only 20% of the total absorbed energy level from Fig. 23.14—the value of \dot{m} obtained using time-resolved spectroscopy should be characteristic of the absorbed intensity in the hot spots. A shift of our experimental points in Fig. 23.15 by a factor of 3 in I_A results in reasonable agreement with code predictions for $f = 0.1$. Under the assumption that the laser

energy distribution on target is the same for the approximately constant diameter targets used in these studies, the measured scaling of \dot{m} with I_A should be valid. Similarly, the discrepancy between the measured and calculated values of the amount of mass ablated during the laser pulse in Fig. 23.14 can be attributed to the burn-through of only small areas of the CH coating generated by the hot spots in the irradiation pattern.

With 12 beams, the irradiation uniformity should be improved, and we do observe a significant decrease in the magnitude of \dot{m} (see Fig. 23.15). Further evidence for the decrease in \dot{m} with the more uniform 12-beam irradiation are the burn-through curves presented in Fig. 23.16, as measured by the time-integrating channel of the x-ray spectrometer.¹⁰ Here we plot the absolute energy in the $\text{Si}^{+12} 1s^2 - 1s2p$ and $\text{Si}^{+13} 1s-3p$ lines as a function of CH overcoat thickness. The 300-Å Au layer on two of the targets was assumed to have an areal mass density equivalent to 0.5 μm of CH, although the effective thickness of the Au layer is greater than this due to radiation cooling in the higher-Z material. The projected burn-through thickness of $\leq 5 \mu\text{m}$ of CH is much less than the 9 μm of CH interpolated at $I_0 = 3 \times 10^{14} \text{ W/cm}^2$ from the 6-beam data.⁶ This difference cannot be accounted for strictly by the difference in burn-through depth between shells and solids since the onset of the Si emission for our data occurs before the peak of the laser pulse, where the differences in \dot{m} are small.

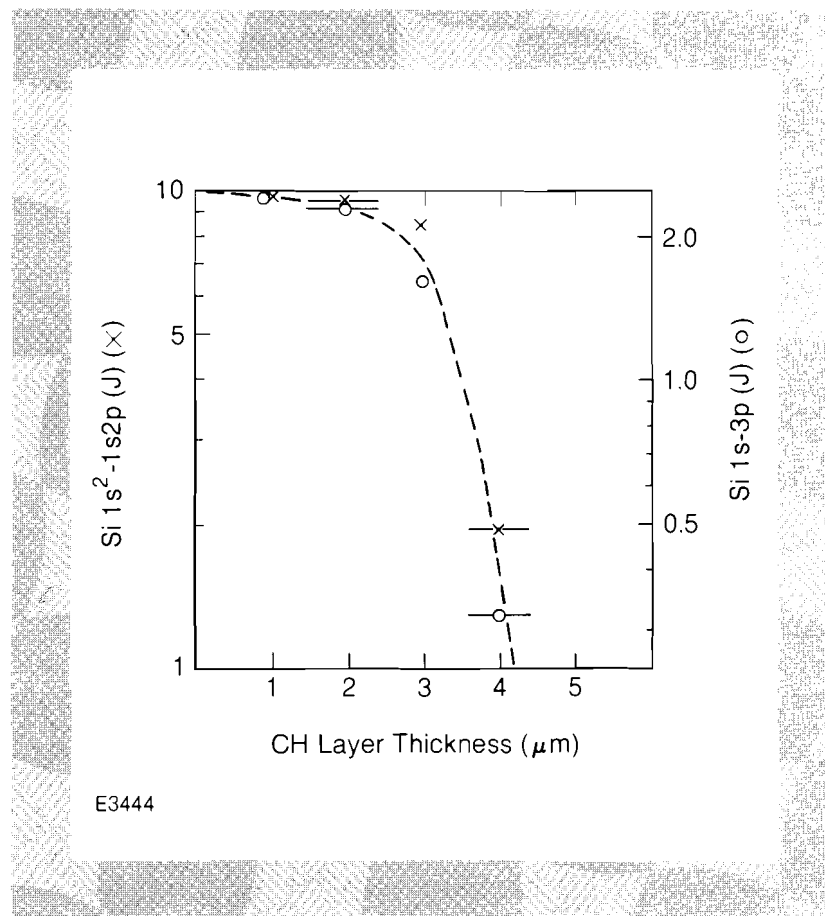


Fig. 23.16
 Burn-through curves for CH and Au/CH on glass targets with 12-beam irradiation at $I_0 = 4 \times 10^{14} \text{ W/cm}^2$ for Si $\text{He}\alpha(x)$ and Si $\text{H}\beta(o)$ x-ray resonance lines.

Although we do not have any direct measurements of the mass-ablation rate on the trailing edge of the laser pulse, we do not observe any Si line emission on the streak records for the 6-beam shots on targets with 6- and 8- μm -thick overcoats of CH. This is consistent with the predicted decrease in \dot{m} that starts before the peak of the laser pulse, as illustrated in Fig. 23.12. Using the timing fiducial method outlined above, we estimate that the onset of the Si line emission for a target with a 4- μm CH overcoat occurs ~ 50 ps before the peak of the laser pulse. If there had been a symmetric scaling of \dot{m} with I_A on the leading and trailing edges of the pulse, we should have observed the Si line emission from the targets with the thicker CH coatings. In addition, if we extrapolate the experimental data in Fig. 23.14 to the mass of these CH layers, the absorbed laser energy on these target shots was sufficient to produce some Si line emission.

Consideration must also be given to the probability of lateral thermal smoothing of the hot spots in the intensity distribution on the target, which appear to dominate the burn-through and \dot{m} measurements with 6-beam irradiation. The amount of smoothing depends on the fractional separation distance $\Delta R/R_0$, where R_0 is the target radius.¹³ For the imploding targets used in this study, the value of $\Delta R/R_0$ is ~ 0.2 by the peak of the laser pulse. A value of ~ 0.3 is predicted by the peak of the laser pulse for the 90- μm -diameter targets irradiated at 10^{15} W/cm² in Ref. 6. It is suggested that the lower scaling of \dot{m} with I_A in Ref. 6 is the result of thermal smoothing. This smoothing decreases the magnitude of \dot{m} to a level more characteristic of the average intensity on target.

Conclusions

The measurement of the mass-ablation rate in spherical geometry with short-wavelength lasers is influenced significantly by time-dependent effects during the laser pulse. The transport of thermal energy, and therefore \dot{m} , is affected by the increasing separation between the energy deposition and ablation surfaces. Irradiation nonuniformities also have a significant effect on mass-ablation-rate measurements using x-ray spectroscopy, as the burn-through seems to be dominated by hot spots. Our experimental measurements of \dot{m} are in agreement with code predictions for the scaling of \dot{m} with I_A on the rising edge of the laser pulse, as shown in Fig. 23.15; only indirect evidence is presented for lower values of \dot{m} on the trailing edge of the laser pulse.

ACKNOWLEDGMENT

This work was supported by the U.S. Department of Energy Office of Inertial Fusion under agreement number DE-FC08-85DP40200 and in collaboration with Los Alamos National Laboratory and Lawrence Berkeley Laboratory under contract number DE-AC03-76SF00098.

REFERENCES

1. C. E. Max, C. F. McKee, and W. C. Mead, *Phys. Fluids* **23**, 1620 (1980).
2. T. J. Goldsack *et al.*, *Phys. Fluids* **25**, 1634 (1982).
3. J. A. Tarvin *et al.*, *Phys. Rev. Lett.* **51**, 1355 (1983).